Journal of Colloid and Interface Science 373 (2012) 1–13

Contents lists available at SciVerse ScienceDirect

Journal of Colloid and Interface Science

www.elsevier.com/locate/jcis

Feature Article, Special Issue: Colloids & Materials 2011

Colloid chemistry of nanocatalysts: A molecular view

Kwangjin An [1], Selim Alayoglu [1], Trevor Ewers, Gabor A. Somorjai *

Department of Chemistry, University of California, Berkeley, California 94720-1460, USA
Chemical Sciences and Materials Sciences Divisions, Lawrence Berkeley National Laboratory, 1 Cyclotron Road, Berkeley, California 94720, USA

ARTICLE INFO

Article history:
Available online 8 December 2011

Keywords:
Colloid
Nanoparticle
Surface
Catalyst
Mesoporous
Turn over
Selectivity
In situ characterization
Sum frequency generation vibrational spectroscopy (SFGVS)
High pressure scanning tunneling microscopy (HPSTEM)

ABSTRACT

Recent advances of a colloidal chemistry can offer great opportunities to fabricate and design nanocatalysts. Comprehensive understanding of a basic concept and theory of the colloidal synthetic chemistry facilitates to engineer elaborate nano-architectures such as bi- or multi-metallic, heterodimers, and core/shell. This colloidal solution technique not only enables to synthesize high surface mesoporous materials, but also provides a versatile tool to incorporate nanoparticles into mesoporous materials or onto substrates. For green chemistry, catalysis research has been pursued to design and fabricate a catalyst system that produces only one desired product (100% selectivity) at high turnover rates to reduce the production of undesirable wastes. Recent studies have shown that several molecular factors such as the surface structures, composition, and oxidation states affect the turnover frequency and reaction selectivity depending on the size, morphology, and composition of metal nanoparticles. Multipath reactions have been utilized to study the reaction selectivity as a function of size and shape of platinum nanoparticles. In the past, catalysts were evaluated and compared with characterizations before and after catalytic reaction. Much progress on *in situ* surface characterization techniques has permitted real-time monitoring of working catalysts under various conditions and provides molecular information during the reaction.

1. Introduction

Colloids and surface chemistry are fields that are often integrated when taught in the chemistry curriculum. The only Division focusing on research in Interface Sciences is called Colloid and Surface Chemistry in the National Meetings of the American Chemical Society held biannually. In recent years both fields have increasingly been defined by research investigations on the molecular level. Colloids have benefitted from the rising importance of nanomaterials, metals and semiconductors that are prepared in colloid solutions in the 1–10 nm size in the forms of nanodots and nanorods [1–3]. Metal catalysts that are usually nanoparticles in the 1–10 nm size range can be synthesized as monodispersed nanoparticles with controlled size and shape using colloid solution techniques. The new catalysts that were generated showed that the catalytic reaction rates, product selectivities and deactivation all change with the size and shape of the metal nanoparticles [4]. Colloid solution techniques can synthesize mesoporous oxides that can be used as metal catalyst supports, bimetallic nanoparticles and core metal–shell oxide systems with novel thermal and chemical properties.

In what appears to be very rapid developments, new catalysts are developed by the synthesis of colloid and catalysis sciences that exhibit unique product selectivity to make a desired product in multipath chemical reactions without waste by-products, which is the aim of "green chemistry."

In this review article, we are reviewing the colloid science approaches to synthesize nanoparticle catalysts of different types. We review the combined development of colloid techniques to produce nanocatalysts and give examples of the unique catalytic chemistry that was achieved. We hope that the reader will share our enthusiasm of this rapidly developing integrated field of colloid and nanocatalysis sciences.

2. Colloidal chemistry for synthesis of nanoparticle and mesoporous materials

2.1. Basic concept of a colloidal synthetic approach

Colloidal synthetic approaches have provided versatile tools for constructing uniform nanomaterials with controlled size, shape and crystalline phase. A variety of methods have been utilized to produce nanoparticles including milling, vapor-phase deposition techniques and solution-based synthesis [1,2]. This section will be focused on colloidal solution-based methods as it is more commonly used in catalytic studies.

* Corresponding author at: Department of Chemistry University of California Berkeley, CA 94720-1460, USA.
E-mail address: somorjai@berkeley.edu (G.A. Somorjai).
[1] These authors contributed equally.

0021-9797/$ - see front matter © 2011 Elsevier Inc. All rights reserved.
doi:10.1016/j.jcis.2011.10.082

General colloidal synthesis primarily consists of three components: reactive precursors for particle formation, surfactants to direct particle size and shape, and solvents to act as a reaction medium. The choice of precursors, surfactants and solvents depend on the material and morphology desired. Typical reaction pathways include thermal decomposition, chemical reduction or oxidation, precipitation, sol–gel and galvanic exchange/replacement [5–8]. For metal nanoparticles, thermal decomposition is often chosen because it can produce small, spherical particles that are monodisperse, having size distributions within 5% ($\sigma_r \leqslant 5\%$). Precursors consist of zero-valent organometallics that are rapidly injected into hot high-boiling solvents with stabilizing surfactants. These reactions are often conducted using standard air-free techniques, as many of the precursors typically used are toxic and/or pyrophoric. Thermal reactions are often conducted at temperatures between 120 °C and 300 °C. Fig. 1 shows a typical reaction setup consisting of a stir-bar, stir plate, heating mantle or oil bath, 3-neck round bottom flask fitted with a septum for injections, a thermocouple and a reflux condenser affixed to an inert gas line and bubbler. Many metal chalcogenides are also made similarly with either the chalcogenide or metal precursor pre-dissolved in the reaction solution before injection. When using ionic precursors, reducing agents may also be needed to produce zero-valent metals or alloys. This allows for the formation of nanoparticles at ambient temperatures or in aqueous solutions. For slow growth, mild reducing agents are used, such as carboxylic acids or thermally activated 1,2-alkanediols. Stronger reducing agents, such as sodium borohydride or superhydride, are required for fast nucleation processes or for metal complexes with very negative reduction potentials.

Surfactants serve to direct particle growth, restrict particle size and stabilize colloidal suspensions to prohibit aggregation and precipitation. These surfactants, also termed ligands, bind onto particles through a surface-interacting functional group and contain a solvent-soluble chain that extends into solution for solubility. A wide variety of surfactants is used and range from organic molecules, polymers to ionic salts. The strength of the interacting functional group and concentration in solution dictates particle size and shape. Covalently interacting groups restrict size and enhance colloid stability, as they are not easily displaced. Weaker electrostatic interactions allow for dynamical adsorption and desorption of ligands within solution to provide greater variability during growth and post-synthetic processing but are more sensitive to environmental perturbation such as changes in ionic strength or dilution. Using multi-dentate ligands can increase the surface interaction for weakly bound functional groups, as is often the case when using polymers. Some common functional groups include carboxylic acids, amines, thiols, phosphines, phosphine oxides, and ammonium and carboxylate salts.

Many ceramic materials are produced using sol–gel processing in which inorganic precursors undergo hydrolysis or polycondensation reactions to form polymer-like extended network structures. This method is often carried out in water/alcohol mixtures and is very sensitive to pH and water/alcohol/precursor ratio. The addition of organic pore directing agents leads to structures with ordered and uniform pore networks. Many synthetic methods for making zeolites, ceramics with ordered pores, require the use of hydrothermal bomb reactors to produce a multiphase solution environment that is ideal for zeolite crystallization [9–12]. Careful drying and calcination techniques are required to ensure structural integrity when forming these zeolites and porous materials [9–11]. These materials are often used in industry as a structural support for metal nanoparticle catalysts and can be modified to enhance catalytic activities or serve as an isomerization catalyst. Current industrial catalysts are primarily formed through deposition or precipitation methods in which metal salts selectively precipitate out of solution onto a supporting material then dried and thermally reduced into small nanoparticles [13,14]. The size and dispersity of the metals on the support is controlled by pH of both the solution and the support. Many supports are intrinsically acidic or basic and provide local environmental differences that facilitate salt deposition. These synthetic methods give greater variations in particle size and local environment and often result in subsurface metal inclusions within the supporting material, which make mechanistic studies difficult [4]. For this reason, the aforementioned colloidal techniques are preferred for studying catalytic pathways on heterogeneous nanoparticle catalysts.

2.2. Formation mechanism of monodisperse nanoparticles

The simplest and often most used model for particle nucleation and growth is the LaMer model in which particle formation is separated into three stages: super-saturation, nucleation and growth [15]. Fig. 2a shows monomer concentration versus reaction progression. In Stage I, monomers are being either formed or added to the solution, yet no particles nucleate despite passing the saturation point. Once the concentration of monomers reach the critical saturation point, particles spontaneously nucleate causing a decrease in particle concentration (Stage II). When the

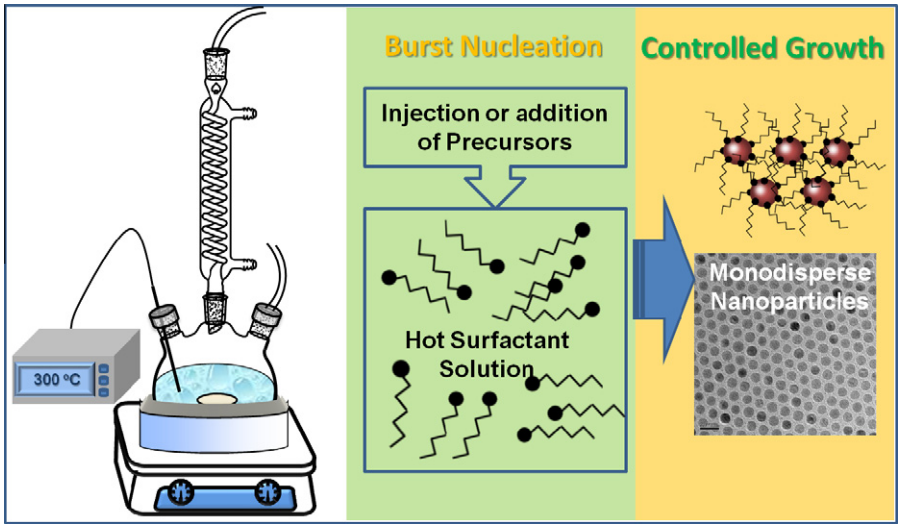

Fig. 1. A typical reaction setup and concept for colloidal synthesis of nanoparticles.

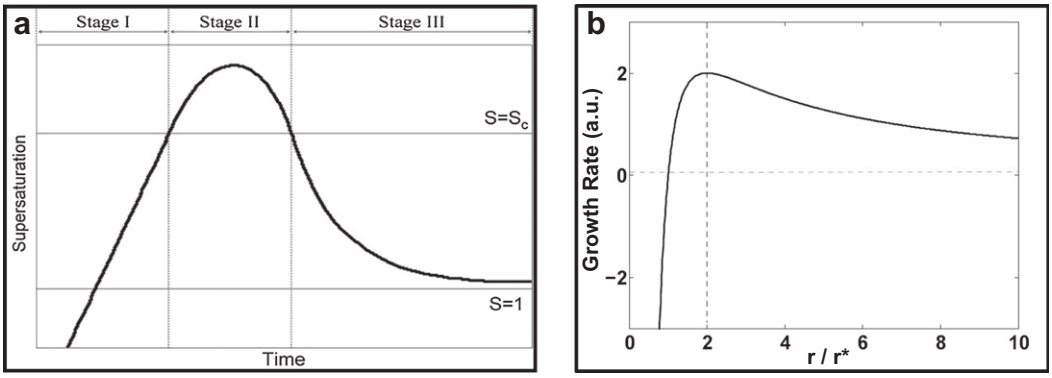

Fig. 2. (a) LaMer plot: Variation of the supersaturation as a function of time (reproduced with permission from [15], copyright 1950 American Chemical Society). (b) Growth model of Sugimoto: Change of the growth rate by the particle size (reproduced with permission from [17], copyright 1987 Published by Elsevier B.V.).

concentration of monomers drop below the critical saturation (Stage III), nucleation of new particles ceases and further monomer loss is obtained solely from particle growth. Because growth will occur simultaneously during particle nucleation, it is important to have a rapid and short nucleation phase and slow growth kinetics to minimize size broadening [16]. Using very reactive precursors and rapidly injecting into a hot coordinating solvent often accomplish this. The reactive precursors decompose quickly, making the nucleation phase short. Residual precursor complexes with the coordinating solvent, forming more stable complexes that will slowly deposit on nuclei for favorable slow growth kinetics. Another method starts with all the desired precursors dissolved in solution at room temperature so that the critical monomer concentration is not reached. Upon heating, the precursors are more reactive and the critical saturation point is lowered just below the monomer concentration causing spontaneous nucleation. This method produces fewer initial nuclei as only a small amount of monomers are used for nucleation resulting in larger average particle sizes. Because only a small amount of monomers are used, the nucleation time is short and growth during this time is minimal [17,18].

For a diffusion controlled growth process, where the precipitation onto a growing particle is limited by the diffusion of monomers to the particle's surface rather than the reaction of the monomers on the particle's surface, two growth regimes exist: a size-focusing regime and a size defocusing regime. These growth processes are governed by the Gibbs-Thompson effect in which the solubility of a particle in relation to its bulk solubility is a function of its size:

$$s_r = s_b \exp(2\sigma V_m / rRT) \quad (1)$$

where s_r and s_b are the solubility of the particle and bulk solid respectively; σ is the specific surface energy; V_m is the molar volume of the material, r is the radius of the particle; R is the gas constant; T is temperature. When $2\sigma V_m/rRT \ll 1$ and the diffusion thickness is considered infinite, the growth rate of particles of size r can be expressed as

$$dr/dt = K(1/r)(1/r^* - 1/r) \quad (2)$$

where K is a rate constant and r^* is the critical particle size for which the growth rate is zero at the current monomer concentration [19,20]. Fig. 2b shows growth rate as a function of particle size r versus the critical particle size r^*. When the average particle size is less than twice the critical particle size, defocusing occurs via an Ostwald's Ripening process in which smaller particles dissolve while larger particles grow more rapidly causing a broadening in the particle size distribution. However, when the average particle size is greater than twice the critical particle size, smaller particles grow at a greater rate than larger particles, leading to a narrowing of the average particle size distribution [21]. At greater monomer concentrations, the critical particle size r^* is smaller. When the super-saturation of monomers is kept high and below the critical saturation point so that no nucleation occurs, size focused growth predominates. For large monodispersed particles, small amounts of monomer are continuously added to maintain high monomer concentrations during long growth times. If the reaction proceeds long enough without further monomer addition, the solution will exit the size-focusing regime and Ostwald Ripening will occur, causing a broadening in the size distribution.

2.3. Strategies for controlling size and shape of nanoparticles

Nanoparticles are synthesized under steric control of surfactants and/or kinetic regulation of nucleation and growth of metal monomers. Thus, one approach to obtain size-controlled nanoparticles is to adjust surfactant concentration [22,23]. For example, a concentrated surfactant solution would result in small particle sizes, whereas larger particles would be obtained in a dilute surfactant solution. This steric control strategy has been previously employed to produce monodisperse gold nanoparticles 1–4 nm in size were synthesized [23–26]. Another strategy for the size control of nanoparticles is to regulate relative rates of nucleation and growth stages. Rhodium nanoparticles ranging 5–13 nm in size have been synthesized by internally adjusting metal precursor concentration [27]. Likewise, the seeded growth strategy is often employed in a two-pot synthesis to increase particle size or deposit metal shells over pre-formed nanoparticle seeds by externally adding additional monomers for growth [28–30]. To avoid homogeneous nucleation of metal monomers, reaction temperature and metal precursor concentration are carefully controlled. The seeded growth technique has been utilized to produce ruthenium and rhodium particles up to 6 nm in size [31,32].

Nanoparticle structure, size and shape are essential to catalysis and can be controlled through colloidal chemistry. The internal structure of a nanoparticle may vary for a given composition, as different crystallographic phases may be kinetically or thermodynamically isolated through colloidal-based synthesis. These structures not only determine the geometry of the surface terminate faces, but may influence the morphology of nanoparticles, as nanoparticle growth is highly influenced by the free-energies of terminal crystallographic faces. For densely packed atomic structures like face-centered cubic (fcc) crystals, {1 1 1} surface termination leads to 8-faced octahedron or 4-faced tetrahedron, whereas (1 0 0) surface termination leads to cubic shapes. Truncated octahedron shapes are resulted from {1 0 0} truncation of octahedron, one special case is cuboctahedron which consists of 6-{1 0 0} tetragonal faces and 8-{1 1 1} hexagonal faces. Further truncation

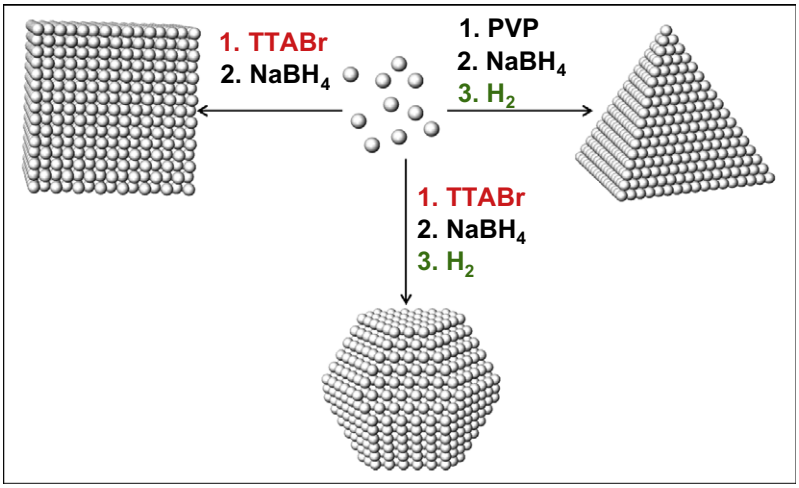

Fig. 3. Schematics illustrate a generic synthetic procedure for preparing Pt nanoparticles with cube, octahedron and cuboctahedron shapes.

exposes higher index surfaces like {1 1 0}, and gives rise to the complex surface structure of polyhedral nanoparticles.

For fcc crystals, {1 1 1} surfaces have the lowest surface free energies and thus are thermodynamically the most stable followed by {1 0 0} and then {1 1 0} surfaces. Since nucleation and growth of nanoparticles are kinetically-controlled by a number of factors such as limited reaction time and temperature, precursor salts and surfactants, nanoparticles usually assumes equilibrium shapes such as truncated cuboctahedron and polyhedron during colloidal chemical synthesis. To synthesize nanoparticles with cubic and tetrahedral (or octahedral) shapes, one approach is to employ surface directing agents along with surfactants. There are vast numbers of surface directing agents at disposal. Namely, alkali and organic salts of halides [33,34], transition metal crystals, cations, and complexes such as Ag^+ [35], Fe^{3+} [36], Co^+ [37], $W(CO)_6$ [38], etc. reactive gas molecules such as H_2, O_2, CO, NO, etc. are noticeable examples of surface directing agents employed in colloidal synthesis of nanoparticles.

In the case of Pt group metal nanoparticles, bromide ions present in the reaction solution produces cubic shapes by stabilizing {1 0 0} surfaces, whereas molecular hydrogen favors tetrahedral shapes with dominantly {1 1 1} surfaces. As shown in Fig. 3, $NaBH_4$ reduction of aqueous solution of H_2PtCl_6 in the presence of tetradecylammonium bromide (TTABr) salt, produced ~15 nm Pt cubes, where TTABr acts as both a surfactant and a surface-directing agent. When dissolved H_2 was employed along with poly-vinylpyrrolidone (PVP) under similar reaction conditions, Pt tetrahedras are formed, which were controllable in the size range of 3–10 nm [39,40]. Also shown in Fig. 3, employing both dissolved H_2 and TTABr solution resulted in ~15 nm Pt cuboctahedras, which is a structural intermediate between cubes and tetrahedras that possesses both {1 0 0} and {1 1 1} faces. Similarly, Ag^+ ions are also known to favor cubic shapes when high concentrations. Exclusively cuboctahedral shapes are formed when trace amounts of Ag^+ ions are present [35].

Recently, it has been shown that size tuning of shape-controlled nanoparticles is possible via colloidal chemical synthesis strategies. For instance, PVP-capped Pt nanocubes in the size range between 5 and 9 nm have been synthesized employing tetramethylammonium bromide (TMABr) as a surface directing agent and the percentage of Pt^{4+} in a Pt^{2+}/Pt^{4+} precursor mixture for size control (Fig. 4) [41]. Pt^{4+} is thermodynamically more difficult to be reduced than Pt^{2+}, and thus fewer Pt nucleates would be initially generated for high Pt^{4+} fractions, leading to larger cubes as residual Pt precursor is reserved for particle growth. Likewise, small Pt cubes are generated with low Pt^{4+} fractions due to fast nucleation of the Pt^{2+} precursor and lower residual Pt ions for further growth.

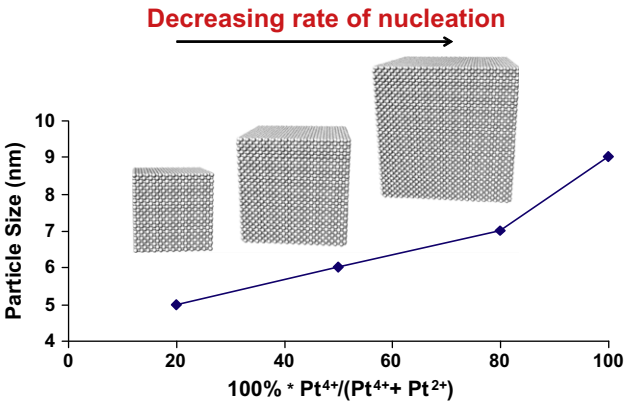

Fig. 4. Particle size of PVP-capped Pt nanocubes are plotted as a function of Pt^{4+} percent in a mixture of Pt^{4+} and Pt^{2+} precursors.

2.4. Mesoporous materials

A mesoporous material is a material containing pores with diameters between 2 and 50 nm. Because of its high surface area, ordered pore structure, and large pore volume, mesoporous materials have been utilized widely as excellent catalyst and support in the field of heterogeneous catalysts [42]. As a porous material, zeolites are also used for ion exchange, adsorption, separation and many catalytic applications [9–11]. However, zeolites – microporous materials whose pore diameters are less than 2 nm –, currently have limited applications for large molecules chemistries due to their narrow pores. Ordered mesoporous materials of the M41S family were first introduced by Mobil R&D Corporation in 1992 (Fig. 5a). Since then, tremendous research on mesoporous materials has been made using self-assembled supramolecular structures of surfactants as a soft template [43]. Self-assembly between inorganic precursors and organic surfactants to form inorganic/organic mesostructures is essential for the formation of mesoporous materials with highly ordered pore structures. Surfactants can be classified mainly into cationic, anionic, and nonionic by their interaction between inorganic precursors and organic surfactants in solutions to form various types of mesostructures such as 2D or 3D hexagonal, 3D cubic, and bicontinuous cubic. These surfactants play a decisive role to design periodic arrangements

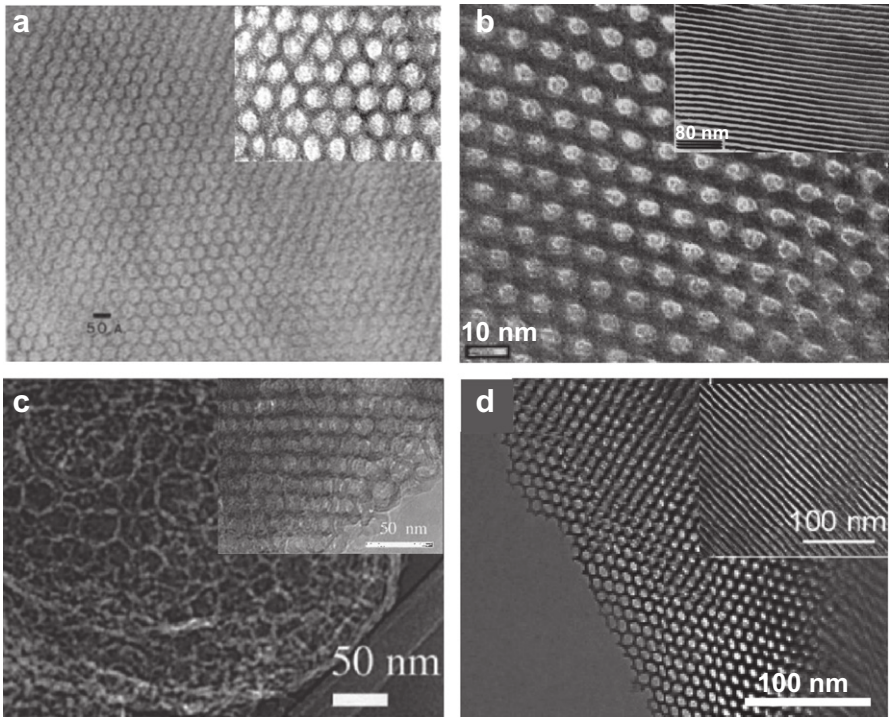

Fig. 5. TEM images of various mesoporous metarials; (a) MCM-41, (b) SBA-15, (c) MCF-17, and (d) alumina (reproduced with permission from [44–46,49], copyright 1992 Nature Publishing Group, copyright 1998 Wiley-VCH, and 1999 and 2008 American Chemical Society).

of pores within mesoporous materials that possess large uniform pore sizes, highly ordered channels, and large surface areas. One of the most popular surfactants is Pluronic P123 (poly(ethylene oxide)$_{20}$-*block*-poly(propylene oxide)$_{70}$-*block*-poly(ethylene oxide)$_{20}$ triblock copolymer), which generates various kinds of mesoporous silica materials such as SBA-15 (Fig. 5b) and MCF-17 (Fig. 5c) by an aqueous sol–gel process using tetraethylorthosilicate (TEOS) as a silica source [44–46]. Both SBA-15 and MCF-17 have been widely used as a support for the preparation of nanocatalysts by incorporating metal nanoparticles into them. While these two kinds of mesoporous silicas are synthesized in a similar way, the MCF-17 has enhanced pore size ranges from 20 to 50 nm as compared to SBA-15 with a size of 6–15 nm. This is accomplished by introducing a pore-swelling agent like trimethylbenzene to expand the mesostructural organic framework.

Since the discovery that oxide-metal interfaces affect catalytic activity and selectivity, much progress has been made to synthesize metal oxide mesoporous materials as a support. Many metal oxides have been produced demonstrating similar geometries as the silicas, including TiO_2, ZrO_2, Al_2O_3, NbO_5, Ta_2O_5, WO_3, SnO as well as mixed oxides [47,48]. Among those metal oxide, mesoporous γ-alumina (γ-Al_2O_3) oxide (Fig. 5d) is chosen as an excellent support due to its acid/base properties and adsorption capacity for many automotive and petroleum industries [49,50].

3. Preparation of nanocatalysts

3.1. 2-D and 3-D catalysts

Colloidal metal nanoparticles can be applied to two types of catalysts; 2-dimensional (2-D) and 3-dimensional (3-D) catalysts [51]. For decades, single crystals have been used for model studies of surfaces and catalysis, both as metal films and supports for metal particles. Similarly, 2-D catalysts are prepared by self-assembled nanoparticles deposited on a substrate by using the Langmuir–Blodgett technique (Fig. 6). Surfactant stabilized colloidal nanoparticles floated on poor solvent – like water for the case of hydrophobic particles – then, assembled to form a closed packed array and deposited on a substrate by emersing the substrate form the liquid.

Conventional industrial catalysts are composed of metal nanoparticles supported on the high surface materials [52]. In order to prepare for industrial heterogeneous catalysts with high surface area, two kinds of methods are mainly adopted: ion-exchange and incipient wetness [13,14]. In both cases, active metal nanoparticles with a size range of 1–10 nm are deposited on and into metal oxides or carbons with high surface area. For ion-exchange, electrostatic interactions between metal precursor and support guarantee high dispersion of nanopaticles, whereas the incipient wetness provides a simple way to obtain nanoparticle catalysts in a large scale by using capillary force to load metal precursors in solution. However, both methods have a broad size distribution of nanoparticles, because of difficulties controlling thermal activation and reduction during the formation of particles on the supports.

Post-synthesis colloidal deposition methods have the advantage of controlled particle size, shape and the elimination of metal adatom inclusions within the support that is often associated with conventional direct deposition methods [52]. The colloidal metal and alloy nanoparticles are incorporated into the pores of mesoporous supports by two methods: capillary inclusion and nanoparticle encapsulation [51]. Via the capillary induced inclusion method, colloidal nanoparticles can be loaded into mesoporous materials by simple sonication in solution (Fig. 6). For example, monodispersed PVP-capped Pt nanoparticles of different sizes (1.7–7.1 nm) were mixed with SBA-15 with a pore diameter of 9 nm in ethanol [53]. Sonication promotes homogenous dispersion of Pt nanopaticles thorough the entire channel of SBA-15 by a capillary force. All Pt sizes were observed to disperse throughout the support forming Pt/SBA-15 3-D nanocatalysts after precipitation and drying. Recently, an alternative approach to effectively

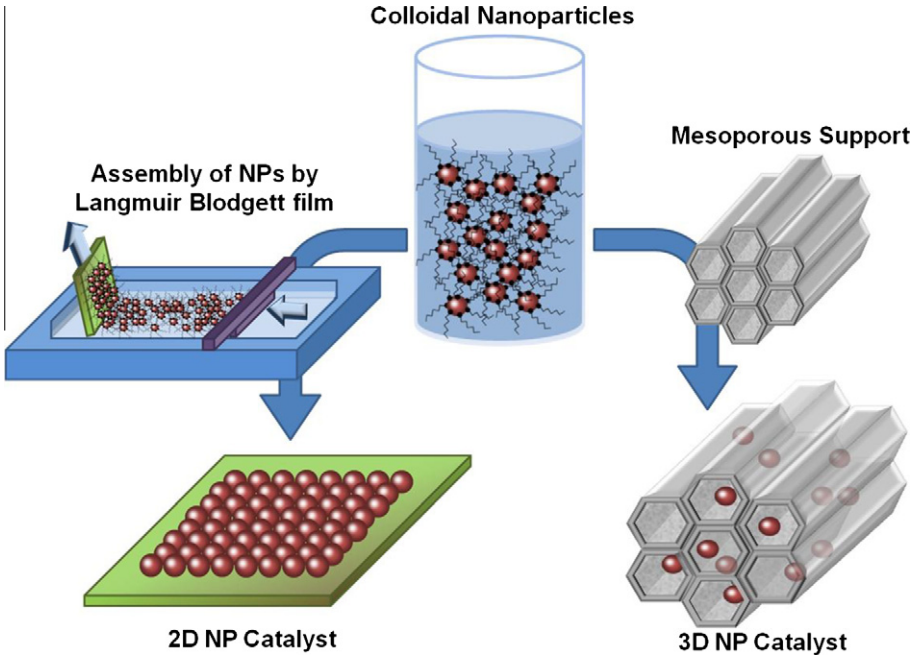

Fig. 6. Schematic illustrations for preparation of colloidal nanopartcle-based 2D and 3D catalysts.

disperse metal nanoparticles within a support involves the direct encapsulation of pre-made metal nanoparticles into a supporting silica matrix during the hydrothermal growth of mesopourous silica. This method is aptly referred to as the nanoparticle encapsulation [54].

3.2. Bimetallic and core/shell nanocatalysts

Bimetallic or core/shell nanoparticles have been developed for engineering catalysts with enhanced activity and selectivity, because they often display composition-dependent surface structure and atomic segregation behavior [4]. The electronic and geometric structures can be tailored by addition of a second metal into the nanoparticle for catalysis. Scheme 1 shows possible bimetallic nanoparticle architectures such as alloy, dimer, core/shell, etc. For example, bimetallic nanoparticles composed of Pt and 3d transition metals such as Fe, Co, Ni, and Cu exhibit high catalytic activity and selectivity as compared to a pure Pt catalyst [55,56]. Through colloidal solution-based approaches, compositionally and structurally controlled bimetallic or multi-metallic nanoparticles have been synthesized. Fig. 7a–c shows bimetallic Rh_xPd_{1-x} nanoparticles synthesized using a one-step colloidal chemistry involving the thermal reduction of two precursors in the presence of surfactant and alcohol. The Rh_xPd_{1-x} nanoparticles undergo reversible changes of surface composition and chemical state [57]. This was due to the surface free energy of the metals and the heat of formation of the metallic oxides in relation to the reaction environment being net oxidizing or net reducing.

Recently, a core/shell Pt/mesoporous silica ($Pt/mSiO_2$) was designed as a thermally stable catalyst [58]. Pt nanoparticles were firstly synthesized as a core through an aqueous reduction of a Pt salt. Then the Pt cores were surrounded by silica shell to generate Pt/SiO_2 nanoparticles using standard sol–gel chemistry. A tetradecyltrimethylammonium bromide (TTAB) capping agent on the Pt cores acted as a pore directing agent upon silica deposition. Upon subsequent calcination, the organic capping agent is removed leaving a mesoporous silica shell behind. During a catalytic reaction, the reactant molecules can access to the surface of Pt cores directly through the mesoporous silica shell. The supporting silica shells not only isolate the catalytically active Pt cores but also prevent the possibility of sintering of core particles during high temperature reactions. $Pt/mSiO_2$ core/shell nanoparticles maintained their structure up to 750 °C and exhibited high catalytic activity for ethylene hydrogenation and CO oxidation.

4. Dynamic behavior of nanoparticles under catalytic reaction conditions

4.1. Structure–surface reactivity relations of metal nanoparticles via catalytic measurements

Because catalysis is a surface phenomenon, particle size and crystallographic shape of nanoparticles often have significant influence on catalytic activity and selectivity for many model and industrial reactions. Hydrogenation reactions of small molecules such as crotonaldehyde, pyrrole, [41,59] furan [60,61] and methylcyclopentane (MCP) [62] were documented to be of a structure-sensitive nature. For example, 10 torr furan and 100 torr H_2 were allowed to react at 80 °C over Pt nanoparticles in the size range between 1 and 7 nm, and a size-dependent surface selectivity was observed (Fig. 8). Small nanoparticles (i.e. 1 nm) produced mainly dihydrofuran, which suggested incomplete hydrogenation of the aromatic ring, whereas butanol was resulted from hydrogenative ring opening of furan over larger nanoparticles (i.e. 7 nm) [60]. Selectivity could also be changed as a function of crystallographic shape. This shape-dependence was observed for methylcyclopentane/H_2 reaction over shape controlled Pt nanoparticles with controlled morphology (Fig. 9) [63]. PVP-capped 6 nm Pt nanoparticles with spherical, cubic, cuboctahedral, and octahedral shapes were synthesized under similar reaction conditions. Each shape exhibits unique faceting to expose different reactive faces. It is well known from single-crystal studies that the exposed crystallographic plane has great influence on catalytic pathways and activities. Hydrogenation of MCP results in ring opening and a subsequent isomerization leads to various C_6 isomers. This reaction pathway was dominant on Pt octahedra

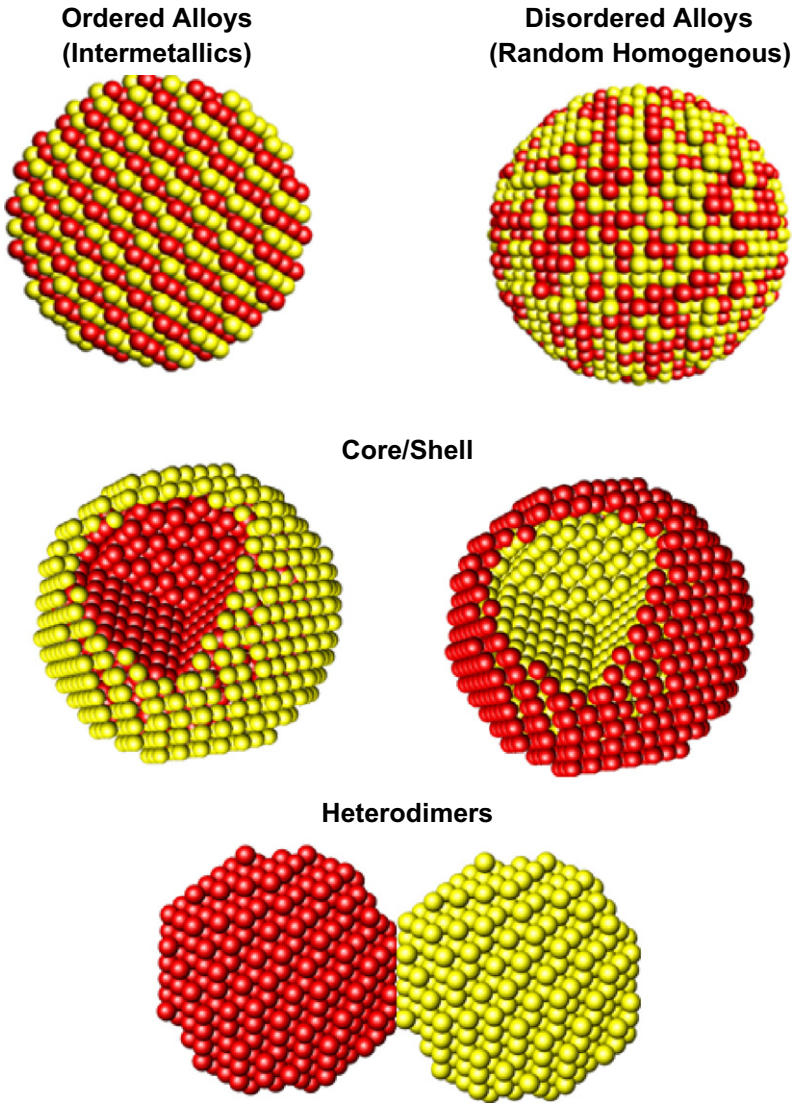

Scheme 1. Possible bimetallic nanoparticle architectures.

(110) and spheres (high index). Octahedra led to hexane and spheres to 2-methylpentane. Further C–C bond breakage gave rise to C_1–C_5 products, and was maxima on Pt cubes (100). At elevated temperatures, C_6 isomers form benzene upon ring closure and subsequent dehydrogenation. This third reaction pathway was dominantly on Pt cubes (100) and Pt cuboctahedra (100) and (111). Given different surface crystallographic orientations, both activity and selectivity exhibited strong shape dependence. Other notable example of shape dependence of surface reactivity is benzene hydrogenation over Pt cubes and cuboctahedra, and has been reported in relation to model single crystal surfaces [62].

4.2. Dynamic in situ characterization of metal nanoparticles surfaces

While catalytic measurements illustrate the importance of particle size and shape on activity, surface-dependant reactions are known to be dynamic processes that may reversibly alter the chemical and structural properties of metals on the surface and, possibly, within the bulk [4]. Oxidation states, intra-metallic distances, average coordination numbers and distribution of atom sites under dynamic reaction conditions are usually different from those of the as-made particles. This necessitated the use of *in situ* tools to characterize metals under catalytically-relevant reaction conditions. A toolbox of instruments and techniques is now available to help uncover surface chemistry and structure as reaction occurs. Surface sum frequency generation vibrational spectroscopy (SFGVS) [64–66], ambient pressure X-ray photoelectron [67,68] and high pressure scanning tunneling microscopy (HPSTM) [69,70] are some of the *in situ* surface techniques. X-ray absorption spectroscopy (XAS) becomes surface specific for cluster-sized particles where bulk becomes surface [71–73].

4.3. Surface sum frequency generation vibrational spectroscopy

Catalytic reactions such as CO/O_2 and C_2H_4/H_2 can be structure insensitive (i.e. on Pt surfaces), meaning the size and shape of metals do not affect the surface reactivity [52]. Such reactions could be employed to probe surface area and number of available metal sites or crystallographic orientation of metal surfaces. FTIR vibrational spectroscopy was frequently used to probe CO/O_2 reaction on Pt group metal surfaces [74,75]. CO adsorbed on surfaces give rise to vibrational fingerprints that are characteristics of metal type and surface chemistry, and thus different from those of gas phase CO molecule [75].

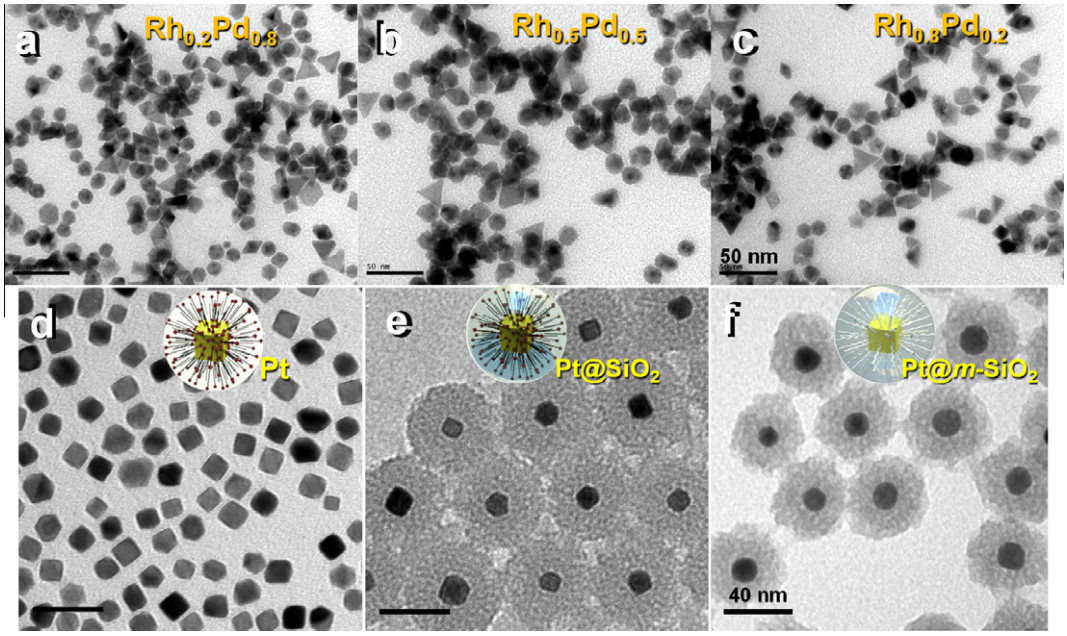

Fig. 7. TEM images of bimetallic and core/shell nanoparticles: (a–c) Ph_xPd_{1-x} nanoparticles. Synthetic procedure from (d) Pt nanoparticles to core/shell (e) Pt/SiO_2, and (f) Pt/mesoporous SiO_2 (reproduced with permission from [58], copyright 2009 Nature Publishing Group).

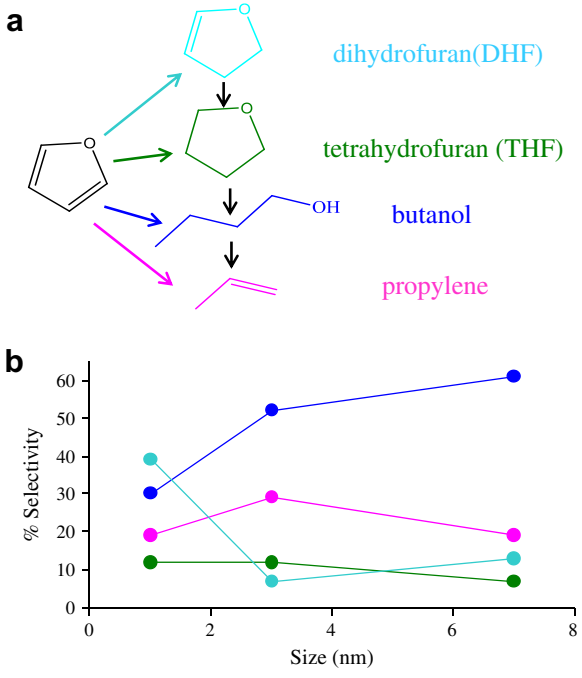

Fig. 8. Reaction scheme of furan hydrogenation showing successive hydrogenation steps (a). % Selectivity for different reaction products, color coded as in (a) as a function Pt particle size (b).

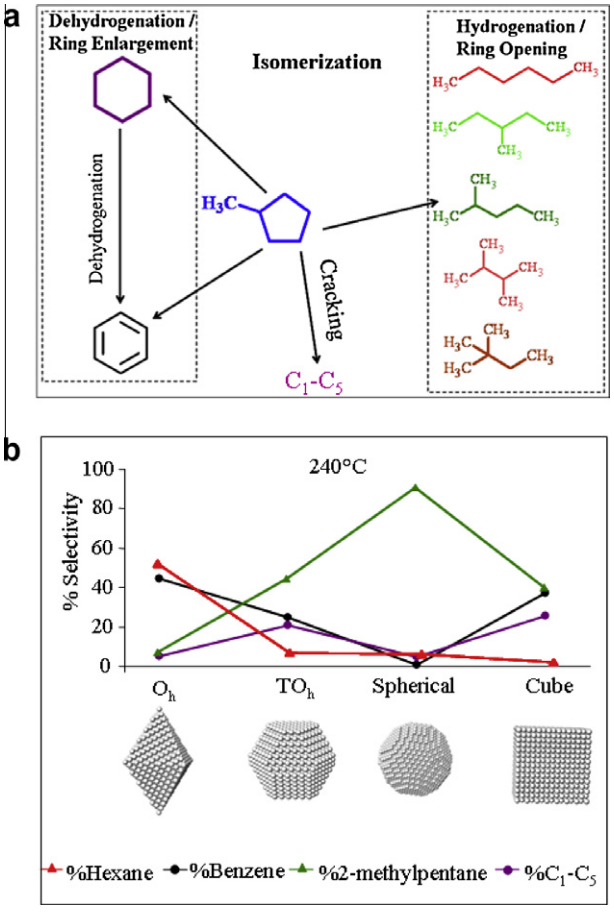

Fig. 9. Reaction scheme of methylcyclopentane hydrogenation showing different reaction pathways and products (a). % Selectivity for different reaction products as a function of Pt particle shapes, (110) octahedron (O_h), truncated octahedron (TO_h), sphere and (100) cube (b). Representative model atom clusters are also given.

4.3.1. SFGVS characterization of surface crystallographic orientations of nanoparticles using ethylene/H_2 probe

It is understood on Pt single crystals that ethylene adsorbate existed in three vibrationally and configurationally distinct states with respect to crystal orientation. Ethylidene, $-CCH_3$ favors three-fold hollow sites of (111) crystal and di-σ-bonded ethylene, $-CH_2CH_2-$ binds to both trigonal (111) and tetragonal hollow sites of (100) (Fig. 10a). In addition, di-σ-bonded ethylene species is

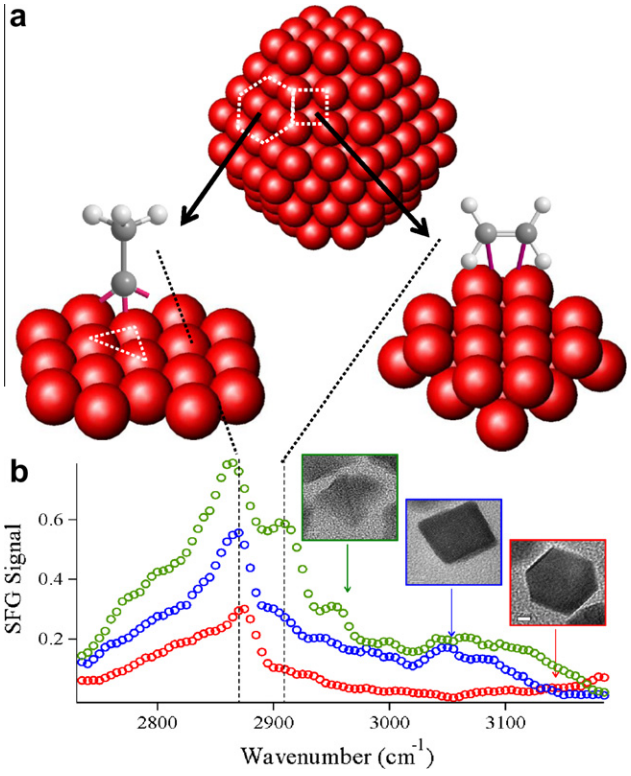

Fig. 10. A truncated octahedron atom cluster is represented with ethylidyne species, $-CCH_3$ on a (1 1 1) terrace and di-σ-bonded ethylene species, $-CH_2H_2C-$ on a (1 0 0) terrace (a). SFGVS spectra in the methyl region shows ethylene adsorbed over Pt nanoparticles with octahedron, cube and truncated octahedron shapes (b). Spectra were collected under 10 torr ethylene and 100 Torr H_2 at 25 °C. Representative TEM pictures of the shape-controlled Pt nanoparticles are also given.

further stabilized on (1 1 0) crystals. SFGVS, for which gas phase molecular vibrations are nullified, could monitor vibrational signatures on the surface at the methyl stretch region. It was this crystal dependence of ethylene adsorption and surface-only detection power of SFGVS that revealed morphological and crystallographic shapes were indeed related for the bulk of Pt nanoparticle colloids. Fig. 10b shows SFGVS spectra of nano-structured Pt cubes, cuboctahedra and octahedra probed by C_2H_4/H_2 reaction, indicating the surface structure/shape association relative to bulk crystallographic faces.

4.3.2. SFGVS investigation of surface-adsorbate states under catalytic reactions

Traditionally, SFGVS was employed to study the catalytic reactions over single crystal surfaces. Hydrogenation of small molecules such as ethylene [65], cyclohexene [76–78], benzene [79–82] crotonaldehyde [83,84], pyrrole [59], etc. was studied using SFGVS and surface adsorbate interactions were well-documented. Surface structure in terms of adsorbate configuration and orientation relative to metal surface was probed at the molecular level and reaction intermediates and spectator molecules were revealed, which revolutionized the way surface science could be studied. Recently, UV/O_2 cleaning of nanoparticle surfaces off capping agents has recently allowed nanoparticle films to be investigated under catalytic reactions [85]. Thus, catalytically relevant colloidal metal nanoparticles were brought into the reach of SFGVS. This constituted another revolution to bridge the materials gap between atomically flat model single crystal surfaces and under-coordinated defect-rich nanoparticle surfaces. SFGVS study of benzene/H_2 reaction over shape controlled Pt nanoparticles with cubic (1 0 0) and cuboctahedral (1 0 0) and (1 1 1) shapes was a milestone in the field, and was soon followed by many others [71,72].

Furan/H_2 reaction provided a bi-functional hydrogenation pathway with distinct spectral fingerprints at the methyl region, and thus ideal for SFGVS studies [60,61]. Catalytic reaction was carried out at 80 °C over Pt nanoparticles in the size range between 1 nm and 7 nm, and revealed that large particles enhanced butanol formation via ring opening, whereas small particles preferentially formed dihydrofuran through partial hydrogenation of the aromatic ring (Fig. 8) [60]. As temperature increased, cracking reaction took over and propylene formed in expense of dihydrofuran and butanol over Pt 1 nm particles. On the other hand, Pt(1 1 1) single crystal surfaces produced no detectable amounts of propylene, but formed butanol, which scaled up with increasing temperatures at and above 100 °C. The structural origin at the molecular level of this surface reactivity trend over Pt single crystals and nanoparticles were investigated using SFGVS. Fig. 11 shows SFG spectrum of Pt 1 nm particles and suggests that surface-adsorbed furan co-existed with the C_4 products at temperatures below 100 °C. At 100 °C and above, methyl stretch intensity due to butanol adsorbate, which bonded through the O atom and was at upright position relative to surface parallel, and dihydrofuran decreased with increasing temperatures. However no spectral feature due to adsorption of propylene was obtained. In corroboration with the catalytic turnover measurements, these observations led to the conclusion that C_4 species cracked to C_3 olefin, CO and H_2 on the defect or under-coordinated atom sites over nanoparticles [60].

4.4. Ambient pressure X-ray photoelectron spectroscopy

When gas atmosphere pressures in the torr regime is combined with energy tunable synchrotron X-rays, X-ray photoelectron spectroscopy (XPS) become a unique tool to study metal nanoparticles under catalytically-relevant reaction conditions [67]. Structural and chemical fundamentals of metal nanoparticles could now be resolved at the atomic level on the surface and in the bulk at temperatures and under that catalytic reactions occur through the use of ambient pressure XPS (APXPS).

4.4.1. Surface chemistry and reactivity correlations by APXPS and parallel catalytic activity measurements

Size dependent activity behavior of CO/O_2 reaction on Rh nanoparticles has recently been uncovered using APXPS technique [86]. Fig. 12a shows the turnover rates relative to Rh foil and absolute activation energy as a function of particle sizes between 2 nm and 11 nm. Activation energy for the CO/O_2 reaction increased exponentially with increasing particle sizes, whereas CO/O_2 reaction rates showed exponential decay at 200 °C and under 100 Torr O_2 and 40 Torr CO. 2 and 7 nm Rh particles were investigated using 510 eV photons at 200 °C under 100 mtorr O_2 and 40 mtorr CO (three orders of magnitude lower pressures than catalytic tests). As shown in Fig. 12b, it was found that 2 nm particles were mainly oxidized under reaction conditions, whereas 7 nm particles were metallic under identical conditions [86]. APXPS revealed a clear correlation between surface chemical compositions (i.e. redox state) and surface reactivity, and thus showed the dynamic nature of metal surfaces at the atomic scale.

4.4.2. Determination of bimetallic nanoparticle architectures and reversible rearrangement of atoms under reactive gas atmospheres by APXPS

Surface dynamics become even more complex for bimetallic nanoparticles. Particle architecture is introduced as the fourth dimension of metal structure along with size, shape and oxidation state. Scheme 1 shows possible bimetallic architectures. Elemental

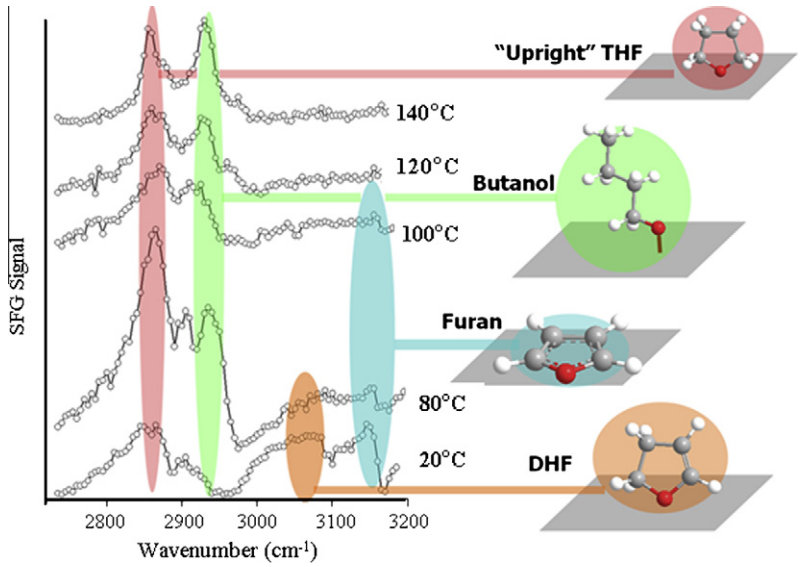

Fig. 11. SFGVS spectra in the methyl region during the furane/H_2 reaction over ~1 nm Pt nanoparticles in the temperature range between 20 °C and 140 °C. The reaction employed 10 Torr furan, 100 torr H_2 and 650 Torr He. Major vibrational peaks were highlighted and corresponding surface configurations were given next to the SFG spectra.

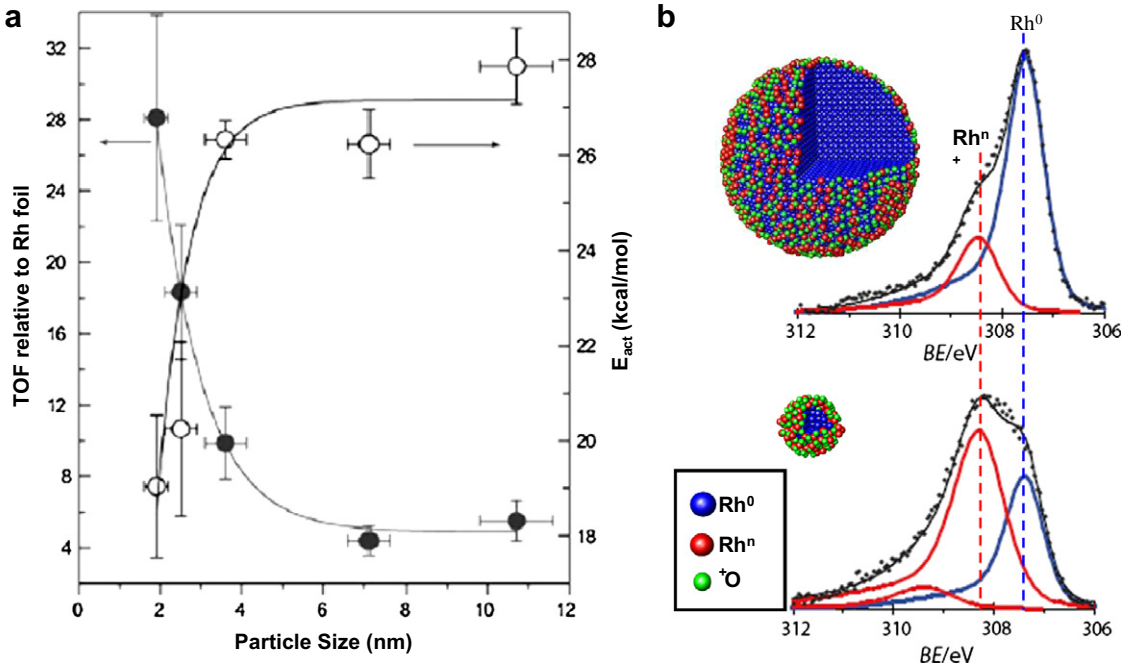

Fig. 12. Plots of TOF relative to Rh foil and activation energy as a function of particle size in the range between 2 nm and 11 nm (a). XP spectra at the Rh5$d^{7/2}$ core level for Rh 2 nm and 7 nm particles. (b). Representative atom clusters with Rh^0 (blue), Rh^{n+} (red) and O (green) are also given next to each XP spectrum.

mapping analogous to STEM/EDS could be obtained using photon energy variable synchrotron XPS technique at vacuum. Therefore, one could determine average particle architecture for any given bimetallic nanoparticle composition. Fig. 13a shows the representative STEM/EDS phase maps and line-scan at Pd L and Rh L edges for a single $Pd_{50}Rh_{50}$ nanoparticle at vacuum [57]. In Fig. 13b, X-ray photoelectron spectra for $Pd_{1-x}Rh_x$ ($x = 0–1$) nanoaparticles at two different photon energies (e.g. Al Kα source at 1486 eV and synchrotron source at 645 eV) revealed surface depletion of Pd at vacuum, in line with STEM/EDS analysis. Having the chemical and structural mobility of metal surfaces in mind, investigation of nanoparticles under dynamic reaction conditions is essential to understanding surface fundamentals and molecular factors that govern catalytic reactions.

$Rh_{50}Pd_{50}$ nanoparticles were subjected to a series of redox cycles at 300 °C, and investigated under APXPS using 645 eV photons [57,68,87]. As shown in Fig. 13c, nanoparticles remained Rh rich in the surface regions under 100 mTorr each of NO and CO atmosphere. On the other hand, Pd segregated to surfaces and formed 50:50 alloys at100 mTorr CO. Moreover, surfaces were switched between Rh rich and 50:50 alloy states back and forth by changing gas environments from oxidizing to net reducing as revealed by APXPS [57,68].

4.5. X-ray absorption spectroscopy at the liquid–metal interface of sub-nanometer Pt clusters

Application of X-ray absorption spectroscopy to heterogeneous catalysis marked a milestone in the field of surface sciences toward

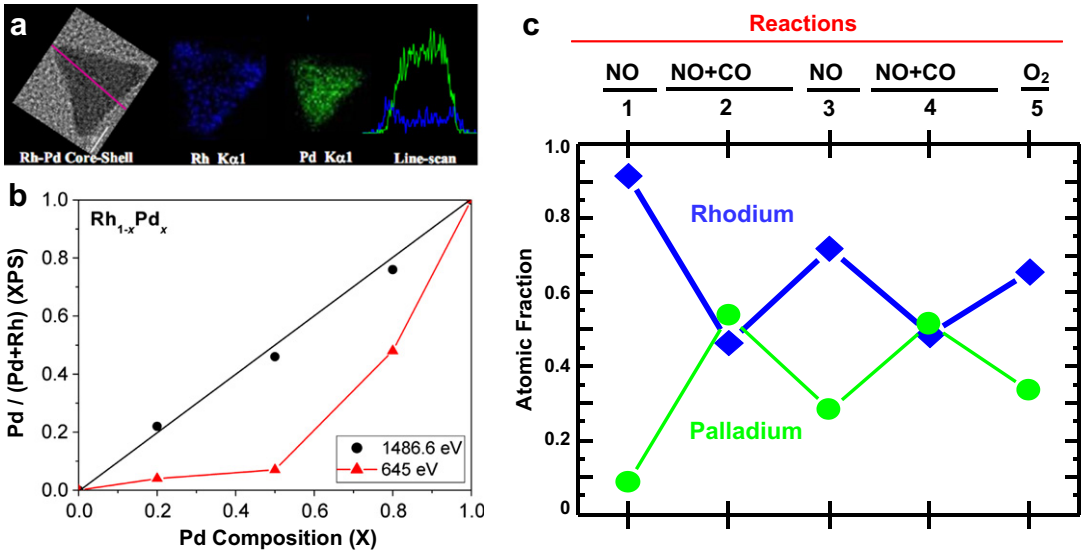

Fig. 13. TEM bright field image, STEM/EDS phase maps and line-scan at the Rh K (blue) and Pd K (green) edges (a). Atomic fraction of Pd on the surface (XPS) as a function of Pd composition in the bulk are shown for photon energies of 1487 eV (Al Kα) and 645 eV (synchrotron) for composition-controlled $Rh_{1-x}Pd_x$ ($x = 0–1$) nanoparticles (b). Atomic fraction of Rh (blue) and Pd (green) measured by APXPS using photon energy of 645 eV as a function of reaction atmosphere (c).

a better understanding of the close and strong relationship between structure and chemistry. In spite of being a bulk probing technique, XAS could be employed for *in situ* and *operando* studies at elevated temperatures and pressures. For the unique case of sub-nanometer clusters, typically 40 atoms and less, surface constitutes >80% of the total atoms. XAS, then, becomes surface specific and measures structural and chemical properties of all catalytically-relevant atoms [71].

An important class of sub-nanometer clusters is dendrimer-encapsulated nanoparticles (DENs) for which, a number of mono-metallic to bimetallic nanoparticle can generically be synthesized using dendrimer templates. Pt DENs have been recently applied to homogeneous catalytic transformation of small molecules, and XAS has been the *in situ* surface characterization tool to study the reaction as it occurs at the liquid–solid interface [88]. Fig. 14a shows the average coordination numbers of Pt–Pt, Pt–O, and Pt–Cl atom pairs for a few redox cycles derived from extended X-ray absorption fine structure (EXAFS) analysis [89]. Reduced clusters had the average coordination numbers of 5 which corresponded to sub-nanometer sized 5–15 atom Pt clusters. When oxidized the average coordination number dropped to 1 which suggested dissolution of clusters into single and isolated ions. Cluster and single atom states could be reinstated back and forth through redox cycles. In agreement with this picture, X-ray absorption near edge spectroscopy (XANES) revealed mainly metallic Pt for the reduction cycles, whereas oxidized Pt in the

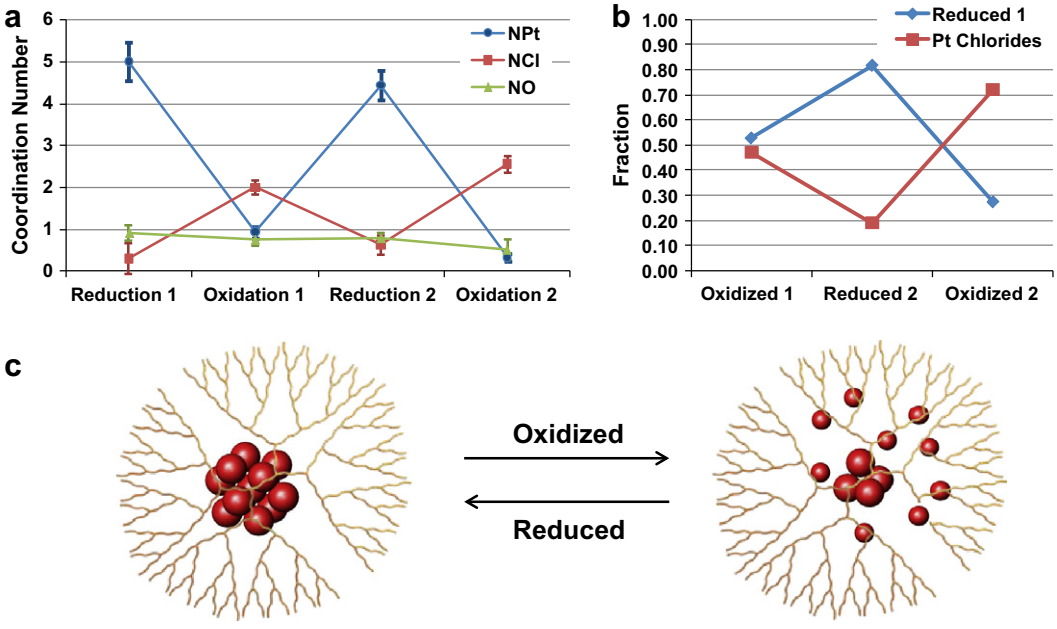

Fig. 14. Average coordination numbers of Pt–Pt, Pt–Cl and Pt–O pairs from EXAFS (a) and fraction of metallic and oxidized (i.e. chlorides) Pt from NEXAFS (b) as a function of redox environment for dendrimer encapsulated Pt nanoparticles supported in SBA15. Schematic illustrates the redox mechanism of dendrimer encapsulated Pt (reproduced with permission from [89], copyright 2011 American Chemical Society).

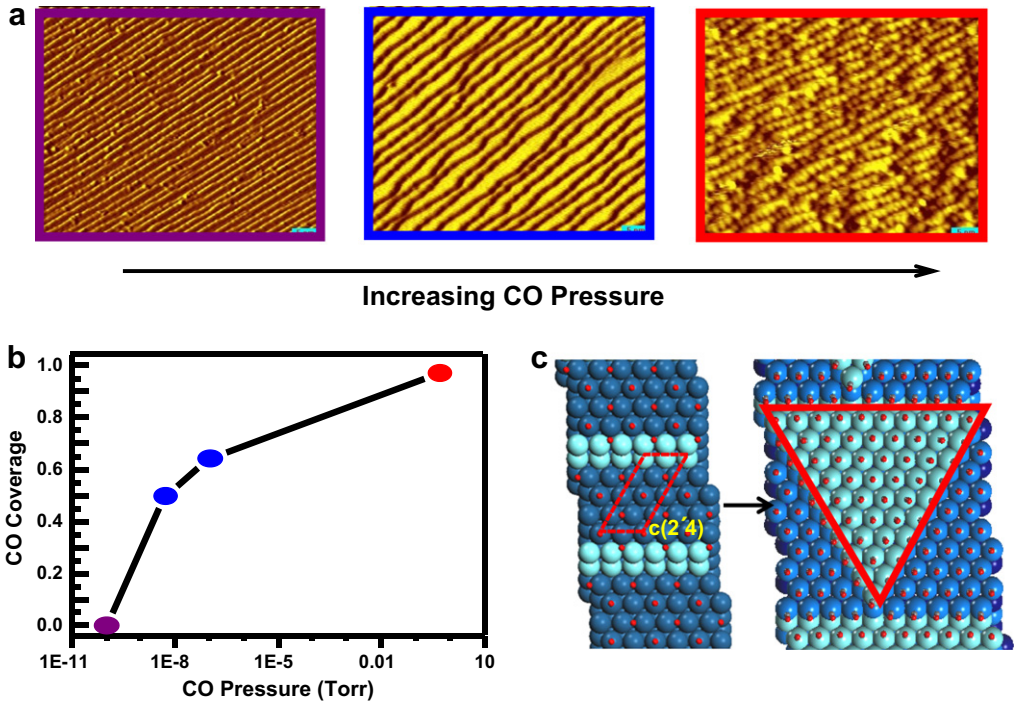

Fig. 15. STM images of a Pt(557) single crystal with increasing CO pressure, stepped surfaces at 10^{-10} Torr, (111)-doubled stepped surfaces at 10^{-8}–10^{-6} Torr and ~2 nm clusters at 1 Torr CO (a). Surface coverage of CO as a function of CO pressures from APXPS (b). DFT snapshots of Pt(557) at low CO coverage and triangulat Pt clusters at saturation coverage of CO (c).

form of chlorides were present for the oxidation cycles (Fig. 7b). Based on the XAS studies, a redox model was derived for the reaction mechanism of a homogeneous molecular transformation at the liquid–metal interface (Fig. 14c).

4.6. High pressure scanning tunneling microscopy study of pressure-dependent clustering of Pt(557)

Low index single crystal surfaces such as (111) and (100) were often employed to study surface aspects of catalytic reactions. Scanning tunneling microscopy (STM) provides a unique way of simultaneously imaging metal surfaces with an interfacial reactive gas adlayer. While STM imaging of nanoparticles synthesized by colloidal chemistry sets a major challenge, investigation of single crystal surfaces with nanoparticle-like faceting provide a model systems for STM studies [90]. Pt(557) single crystal has stepped surfaces composed of Pt(111) terraces and Pt(100) steps, and thus mimics nanoparticles with statistically significant numbers of corner and edge atoms [91].

Pt(557) surfaces were studied using STM at CO pressures from UHV to Torr regime, and CO pressure-induced restructuring and clustering of Pt(557) was investigated [91]. At 10^{-10} Torr CO and 25 °C, STM showed Pt(111) terraces (Fig. 15a). APXPS revealed no CO adsorption (i.e. 0 surface coverage) under identical conditions (Fig. 15b). When CO pressure was increased to 10^{-8} Torr Pt(111) terraces were doubled in length while surface coverage of CO reached 0.5. At 1 Torr CO, Pt(557) steps were restructured and broke up into small Pt clusters of approximately 2 nm particle sizes. CO reached its saturation coverage on Pt at 1 Torr. Based on the experimental findings, density functional theory (DFT) calculations were carried out, and predicted clustering of Pt(557) single crystal at high CO coverage due to strong CO-CO repulsion (Fig. 15c). It was also documented that Pt(111) terraces were restored at 10^{-8} Torr CO after 1 Torr CO gas was pumped out. In summary, HPSTM revealed pressure-dependent mobility of Pt surfaces with edges and terraces, and helped bridging the pressure gap in the case of CO adsorption over Pt.

5. Conclusions and outlook

Colloidal solution based nanotechnology has been developed to control nanomaterial size, shape, composition, uniformity, and functionality. Industrial catalysts have targeted nanomaterials with controlled size and shape, as nanoparticles have high surface areas that provide more active sites to lower activation energy for catalytic reactions. In addition, shape selectivity provides unique surface structures—such as steps, kinks and terraces—to influence reaction pathways leading to product selectivity. Recent results show that turnover rates and selectivity of catalytic reactions can be influenced by the size and shape of nanoparticles as their surface structures and active sites are tailored at the molecular level. Nanoparticles lie within the transitional size regime, which make them highly suitable for tuning catalytic properties for robust, selective and highly active catalysts. Our group has demonstrated that several molecular factors govern the activity and selectivity of shape dependent nanoparticle catalysts including: surface structure and composition of nanoparticles, reaction intermediates, adsorbates, and oxidation states. Advanced *in situ* and *ex situ* characterization techniques have permitted the study of dynamic behaviors under catalytic reactions. The colloidal synthetic approach has enabled the control of the size, shape, and composition of nanoparticle precisely, while advances in *in situ* characterization techniques have allowed the monitoring of dynamic behavior of catalysts during reactions. The utilization of advanced synthetic procedures, characterizations, and reaction studies opens new possibilities for the design of ideal "green catalysts" exhibiting near 100% selectivity, maximal activity, and long-term stability.

Acknowledgments

This work was supported by a grant from Chevron Corp. and Honda Research and Development. We also acknowledge support by the Director, Office of Science, Office of Basic Energy Sciences, Division of Materials Sciences and Engineering of

the US Department of Energy under Contract No. DE-AC02-05CH11231.

References

[1] G. Schmid, Nanoparticle: From Theory to Application, Wiley-VCH, Weinheim, 2004.
[2] K.J. Klabunde, Nanoscale Materials in Chemistry, Wiley-Interscience, New York, 2001.
[3] C.M. Niemeyer, C.A. Mirkin, Nanobiotechnology: Concept, Applications and Perspectives, Wiley-WCH, Weinheim, 2004.
[4] G.A. Somorjai, J.Y. Park, Angew. Chem., Int. Ed. 47 (2008) 9212.
[5] Y.W. Jun, J.S. Choi, J. Cheon, Chem. Commun. (2007) 1203.
[6] J. Park, J. Joo, S.G. Kwon, Y. Jang, T. Hyeon, Angew. Chem., Int. Ed. 46 (2007) 4630.
[7] S.E. Skarabalak, J. Chen, Y. Sun, X. Lu, L. Au, C.M. Cobley, Y. Xia, Acc. Chem. Res. 41 (2008) 1587.
[8] X. Wang, Q. Peng, Y.D. Li, Acc. Chem. Res. 40 (2007) 635.
[9] G.J.A.A. Soler-Illia, C. Sanchez, B. Lebeau, J. Patarin, Chem. Rev. 102 (2002) 4093.
[10] A. Navrotsky, O. Trofymluk, A.A. Levchenko, Chem. Rev. 109 (2009) 3885.
[11] A. Corma, Chem. Rev. 97 (1997) 2373.
[12] Y. Tao, H. Kanoh, L. Abrams, K. Kaneko, Chem. Rev. 106 (2006) 896.
[13] G. Ertl, H. Knözinger, J. Weitkamp, Handbook of Heterogeneous Catalysis, Wiley-WCH, Weinheim, 1997.
[14] J.W. Geus, J.A.R. van Ween, in: J.A. Moulijn, P.W.N.M. van Leeuwen, R.A. van Santen (Eds.), Catalysis: An Integrated Approach to Homogeneous, Heterogeneous and Industrial Catalysis, Elsevier, Amsterdam, 1993 (Chapter 9).
[15] V.K. Lamer, R.H. Dinegar, J. Am. Chem. Soc. 72 (1950) 4847.
[16] Y. Yin, A.P. Alivisatos, Nature 437 (2005) 664.
[17] T. Sugimoto, Adv. Colloid Interface 28 (1987) 65.
[18] T. Sugimoto, Monodispersed Particles, Elsevier, Amsterdam, 2001.
[19] R. Xie, Z. Li, X. Peng, J. Am. Chem. Soc. 131 (2009) 15457.
[20] E.E. Finney, R.G. Finke, J. Colloid. Interface Sci. 317 (2008) 351.
[21] X.G. Peng, J. Wickham, A.P. Alivisatos, J. Am. Chem. Soc. 120 (1998) 5343.
[22] N.R. Jana, Y.F. Chen, X.G. Peng, Chem. Mater. 16 (2004) 3931.
[23] G. Mpourmpakis, S. Caratzoulas, D.G. Vlachos, Nano. Lett. 10 (2010) 3408.
[24] M.-C. Daniel, D. Astruc, Chem. Rev. 104 (2004) 293.
[25] X.M. Lin, H.M. Jaeger, C.M. Sorensen, K.J. Klabunde, J. Phys. Chem. B 405 (2001) 3353.
[26] Z.X. Wang, B.E. Tan, I. Hussain, N. Schaeffer, M.F. Wyatt, M. Brust, A.I. Cooper, Langmuir 23 (2007) 885.
[27] Y.W. Zhang, M.E. Grass, S.E. Habas, F. Tao, T.F. Zhang, P. Yang, G.A. Somorjai, J. Phys. Chem. C 111 (2007) 12243.
[28] S.M. Humphrey, M.E. Grass, S.E. Habas, K. Niesz, G.A. Somorjai, T.D. Tilley, Nano. Lett. 7 (2007) 785.
[29] K. Lee, M. Kim, H. Kim, J. Mater. Chem. 20 (2010) 3791.
[30] A. Seyed-Razavi, I.K. Snook, A.S. Barnard, J. Mater. Chem. 20 (2010) 416.
[31] S. Alayoglu, B. Eichhorn, J. Am. Chem. Soc. 130 (2008) 17479.
[32] S.H. Joo, J.Y. Park, J.R. Renzas, D.R. Butcher, W. Huang, G.A. Somorjai, Nano. Lett. 10 (2010) 2709.
[33] T.H. Ha, H.J. Koo, B.H. Chung, J. Phys. Chem. C 111 (2007) 1123.
[34] Y.W. Zhang, M.E. Grass, J.N. Kuhn, F. Tao, S.E. Habas, W.Y. Huang, P.D. Yang, G.A. Somorjai, J. Am. Chem. Soc. 130 (2008) 5868.
[35] H. Song, F. Kim, S. Connor, G.A. Somorjai, P.D. Yang, J. Phys. Chem. B 109 (2005) 188.
[36] Y.J. Xiong, J.Y. Chen, B. Wiley, Y.A. Xia, Y.D. Yin, Z.Y. Li, Nano. Lett. 5 (2005) 1237.
[37] S.I. Lim, I. Ojea-Jimenez, M. Varon, E. Casals, J. Arbiol, V. Puntes, Nano. Lett. 10 (2010) 964.
[38] J. Zhang, J.Y. Fang, J. Am. Chem. Soc. 131 (2009) 18543.
[39] Y.T. Yu, B.Q. Xu, Appl. Organomet. Chem. 20 (2006) 638.
[40] J.M. Petroski, Z.L. Wang, T.C. Green, M.A. El-Sayed, J. Phys. Chem. B 102 (1998) 3316.
[41] C.K. Tsung, J.N. Kuhn, W.Y. Huang, C. Aliaga, L.I. Hung, G.A. Somorjai, P. Yang, J. Am. Chem. Soc. 131 (2009) 5816.
[42] Y. Wan, D. Zhao, Chem. Rev. 107 (2007) 2821.
[43] C.T. Kresge, M.E. Leonowicz, W.J. Roth, J.C. Vartuli, J.S. Beck, Nature 359 (1992) 710.
[44] D.Y. Zhao, J.L. Feng, Q.S. Huo, N. Melosh, G.H. Fredrickson, B.F. Chmelka, G.D. Stucky, Science 279 (1998) 548.
[45] D.Y. Zhao, P. Yang, N. Melosh, J. Feng, B.F. Chmelka, G.D. Stucky, Adv. Mater. 10 (1998) 1380.
[46] P. Schmidt-Winkel, W.W. Lukens, D.Y. Zhao, P. Yang, B.F. Chmelka, G.D. Stucky, J. Am. Chem. Soc. 121 (1999) 254.
[47] P. Yang, D. Zhao, D. Margolese, B. Chmelka, G. Stucky, Nature 396 (1998) 152.
[48] Y. Wan, H. Yang, D. Zhao, Acc. Chem. Res. 39 (2006) 423.
[49] Q. Yuan, A.-X. Yin, C. Luo, L.-D. Sun, Y.-W. Zhang, W.-T. Duan, H.-C. Liu, C.-H. Yan, J. Am. Chem. Soc. 130 (2008) 3465.
[50] S.M. Morris, P.F. Fulvio, M. Jaroniec, J. Am. Chem. Soc. 130 (2008) 15210.
[51] G.A. Somorjai, S.H. Joo, in: I. Halasz, (Ed.), Transworld Research Network, Kerala, India, 2010.
[52] G.A. Somorjai, Introduction to Surface Chemistry and Catalysis, Wiley, 1994.
[53] R.M. Rioux, H. Song, J.D. Hoefelmeyer, P. Yang, G.A. Somorjai, J. Phys. Chem. B 109 (2005) 2192.
[54] H. Song, R.M. Rioux, J.D. Hoefelmeyer, R. Komor, K. Niesz, M. Grass, P. Yang, G.A. Somorjai, J. Am. Chem. Soc. 128 (2006) 3027.
[55] V.R. Stamenkovic, B. Fowler, B.S. Mun, P.N. Ross, C.A. Lucas, N.M. Markovic, Science 315 (2007) 493.
[56] L.E. Murillo, A.M. Goda, J.G. Chen, J. Am. Chem. Soc. 129 (2007) 7101.
[57] F. Tao, M.E. Grass, Y.W. Zhang, D.R. Butcher, F. Aksoy, S. Aloni, V. Altoe, S. Alayoglu, J.R. Renzas, C.K. Tsung, Z.W. Zhu, Z. Liu, M. Salmeron, G.A. Somorjai, J. Am. Chem. Soc. 132 (2010) 8697.
[58] S.H. Joo, J.Y. Park, C.K. Tsung, Y. Yamada, P. Yang, G.A. Somorjai, Nat. Mater. 8 (2009) 126.
[59] C.J. Kliewer, M. Bieri, G.A. Somorjai, J. Phys. Chem. C 112 (2008) 11373.
[60] C.J. Kliewer, C. Aliaga, M. Bieri, W.Y. Huang, C.K. Tsung, J.B. Wood, K. Komvopoulos, G.A. Somorjai, J. Am. Chem. Soc. 132 (2010) 13088.
[61] C. Aliaga, C.K. Tsung, S. Alayoglu, K. Komvopoulos, P.D. Yang, G.A. Somorjai, J. Phys. Chem. C 115 (2011) 8104.
[62] F. Zaera, D. Godbey, G.A. Somorjai, J. Catal. 101 (1986) 73.
[63] S. Alayoglu, C. Aliaga, C. Sprung, G.A. Somorjai, Catal. Lett. 141 (2011) 914.
[64] P.S. Cremer, B.J. Mcintyre, M. Salmeron, Y.R. Shen, G.A. Somorjai, Catal. Lett. 34 (1995) 11.
[65] P. Cremer, C. Stanners, J.W. Niemantsverdriet, Y.R. Shen, G. Somorjai, Surf. Sci. 328 (1995) 111.
[66] Y.R. Shen, Nature 337 (1989) 519.
[67] D.F. Ogletree, H. Bluhm, G. Lebedev, C.S. Fadley, Z. Hussain, M. Salmeron, Rev. Sci. Instrum. 73 (2002) 3872.
[68] F. Tao, M.E. Grass, Y.W. Zhang, D.R. Butcher, J.R. Renzas, Z. Liu, J.Y. Chung, B.S. Mun, M. Salmeron, G.A. Somorjai, Science 322 (2008) 932.
[69] B.J. Mcintyre, M. Salmeron, G.A. Somorjai, J. Vac. Sci. Technol., A 11 (1993) 1964.
[70] B.J. Mcintyre, M. Salmeron, G.A. Somorjai, Rev. Sci. Instrum. 64 (1993) 687.
[71] M.S. Nashner, A.I. Frenkel, D.L. Adler, J.R. Shapley, R.G. Nuzzo, J. Am. Chem. Soc. 119 (1997) 7760.
[72] M.S. Nashner, A.I. Frenkel, D. Somerville, C.W. Hills, J.R. Shapley, R.G. Nuzzo, J. Am. Chem. Soc. 120 (1998) 8093.
[73] S. Reimann, J. Stotzel, R. Frahm, W. Kleist, J.D. Grunwaldt, A. Baiker, J. Am. Chem. Soc. 133 (2011) 3921.
[74] J.A. Rodriguez, C.M. Truong, D.W. Goodman, J. Chem. Phys. 96 (1992) 7814.
[75] Y. Wang, N. Toshima, J. Phys. Chem. B 101 (1997) 5301.
[76] X.C. Su, K.Y. Kung, J. Lahtinen, Y.R. Shen, G.A. Somorjai, J. Mol. Catal. A: Chem. 141 (1999) 9.
[77] K.M. Bratlie, L.D. Flores, G.A. Somorjai, Surf. Sci. 599 (2005) 93.
[78] M.C. Yang, R.M. Rioux, G.A. Somorjai, J. Catal. 237 (2006) 255.
[79] K.M. Bratlie, L.D. Flores, G.A. Somorjai, J. Phys. Chem. B 110 (2006) 10051.
[80] K.M. Bratlie, C.J. Kliewer, G.A. Somorjai, J. Phys. Chem. B 110 (2006) 17925.
[81] K.M. Bratlie, H. Lee, K. Komvopoulos, P. Yang, G.A. Somorjai, Nano. Lett. 7 (2007) 3097.
[82] K.M. Bratlie, Y.M. Li, R. Larsson, G.A. Somorjai, Catal. Lett. 121 (2008) 173.
[83] M. Grass, R. Rioux, G. Somorjai, Catal. Lett. 128 (2009) 1.
[84] C.J. Kliewer, M. Bieri, G.A. Somorjai, J. Am. Chem. Soc. 131 (2009) 9958.
[85] C. Aliaga, J.Y. Park, Y. Yamada, H.S. Lee, C.K. Tsung, P. Yang, G.A. Somorjai, J. Phys. Chem. C 113 (2009) 6150.
[86] M.E. Grass, Y.W. Zhang, D.R. Butcher, J.Y. Park, Y.M. Li, H. Bluhm, K.M. Bratlie, T.F. Zhang, G.A. Somorjai, Angew. Chem., Int. Ed. 47 (2008) 8893.
[87] J.R. Renzas, W.Y. Huang, Y.W. Zhang, M.E. Grass, G.A. Somorjai, Catal. Lett. 141 (2011) 235.
[88] C.A. Witham, W.Y. Huang, C.K. Tsung, J.N. Kuhn, G.A. Somorjai, F.D. Toste, Nat. Chem. 2 (2010) 36.
[89] Y. Li, J.H.-C. Liu, C.A. Witham, W. Huang, M.A. Marcus, S.C. Fakra, P. Alayoglu, Z. Zhu, C.M. Thompson, A. Arjun, K. Lee, E. Gross, F.D. Toste, G.A. Somorjai, J. Am. Chem. Soc. 113 (2011) 13527.
[90] G.A. Somorjai, J.Y. Park, Chem. Soc. Rev. 37 (2008) 2155.
[91] F. Tao, S. Dag, L.W. Wang, Z. Liu, D.R. Butcher, H. Bluhm, M. Salmeron, G.A. Somorjai, Science 327 (2010) 850.